

Modeling vertical motion at ocean fronts: Are nonhydrostatic effects relevant at submesoscales?

Amala Mahadevan*

Department of Earth Sciences, Boston University, 685 Commonwealth Avenue, Boston, MA 02215, USA

Received 14 August 2005; received in revised form 25 May 2006; accepted 26 May 2006

Available online 30 June 2006

Abstract

Through a suite of three-dimensional, high-resolution numerical modeling experiments, we examine the role of nonhydrostatic effects on $O(1\text{ km})$ submesoscale processes at ocean fronts, with particular focus on the vertical velocity field. Several differences between nonhydrostatic and hydrostatic models are pointed out using a framework that enables precise comparison, but it is difficult to identify categorical differences between the model solutions at the grid resolutions afforded. The instantaneous vertical velocity structure is sensitive to the model choice and, even more so, to grid resolution, but the average vertical flux is similar in both hydrostatic and nonhydrostatic cases.

When a frontal region with horizontal density gradients is perturbed by wind, a profusion of submesoscale, $O(1\text{ km})$, secondary circulation features develops in the upper 50 m. Narrow, elongated cells of intense up- and down-welling are found to occur close to the surface, overlying broader regions of weaker up- and down-welling associated with the mesoscale meanders of the baroclinically unstable front. The submesoscale down-welling is considerably stronger than up-welling and is concentrated in 1–2 km width filaments within which velocities can attain magnitudes as high as 200 m day^{-1} . The submesoscale features are found to be robust at horizontal grid resolutions varying between 1 and 0.25 km and exist even in the hydrostatic model. Submesoscale circulation is difficult to observe or resolve in coarser resolution circulation models, but is likely to play a significant role in the exchange of energy and properties between the surface ocean and thermocline. Possible mechanisms for the generation of these features are investigated in a follow-on paper.

© 2006 Elsevier Ltd. All rights reserved.

1. Introduction

At large scales, oceanographic flows are largely two dimensional. The vertical component of the fluid velocity is typically smaller than the horizontal component by several (typically 4–5) orders of magnitude. This is because the geometrical aspect (depth to length) ratio of the oceans is very small and the effect of the earth's rotation and density stratification further inhibit vertical motion. On the large, synoptic, $\sim 1000\text{ km}$ scale, as well as on the $\sim 10\text{--}100\text{ km}$ scale of eddies and frontal meanders, namely the mesoscale, flows are

* Tel.: +1 6173535511; fax: +1 6173533290.

E-mail address: amala@bu.edu

largely in hydrostatic and geostrophic balance and the Rossby number and aspect ratio are typically $\ll 1$. In the nearly two-dimensional flows that result, energy cascades up scale and dissipation is not achieved through three-dimensional turbulence. In contrast, much smaller scaled oceanic phenomena, typically $\leq O(100\text{ m})$, such as the breaking of internal waves, convection, and shear-induced overturning, are three-dimensional in character. They result in energy dissipation and contribute to diapycnal mixing in the ocean. A major conundrum (McWilliams, 2003) is that the highly energetic mesoscale flow field is largely non-dissipative, and the smaller scale three-dimensional motions are inadequate to account for the diapycnal mixing that is required to balance the budget of energy and tracer fluxes in the oceans (Wunsch and Ferrari, 2004).

The focus here is on the *submeso* $O(1\text{ km})$ scale, which is intermediate to the *meso* scale that is characteristic of eddies and meanders, and the scale of fully three-dimensional motion (henceforth referred to as the *small* scale). Instabilities that occur at submeso scales may facilitate the transfer of energy from meso to small scales (McWilliams, 2003; Molemaker et al., 2005). In numerical modeling studies of mesoscale flows performed at increasingly higher grid resolutions, we find the existence of localized regions $O(1\text{ km})$ in horizontal extent, in which the magnitude of the vertical velocity becomes large. It is feasible that in these regions, the familiar geostrophic and hydrostatic balances are weakened, and as the local Rossby number and aspect ratio tend to approach $O(1)$, quasi three-dimensional motion is generated. In the numerical model, features with relatively strong vertical velocities are observed in filamentous edge- and cusp-like features at oceanic fronts, particularly in the presence of wind forcing or topographic variations. The effects of these submesoscale motions are largely unknown, but need to be investigated because they may cumulatively affect oceanic diapycnal transport, the dissipation of energy input at the surface, the spontaneous breakdown of mesoscale structures, and the distribution of properties in the ocean. Further, these motions may be the link between non-dissipative mesoscale flows and dissipative three-dimensional motion.

Density fronts in the upper ocean are likely sites for such submesoscale activity. They are associated with narrow geostrophic jets and strong shear, exist over a range of scales (Ferrari and Rudnick, 2000), and are ubiquitous (Ullman and Cornillon, 1999) to the oceans. Upper ocean fronts are instrumental in facilitating the exchange of properties between the surface ocean and upper thermocline. It is the intensity of frontal, up- and down-welling motions that sets the rates of exchange (of nutrients for phytoplankton, dissolved carbon dioxide, oxygen, etc.) in the vertical, particularly beyond the reach of the mixed layer. Within the mixed layer, mixing induced by wind, convection and shear, plays the role of actively homogenizing properties, but submesoscale vertical motion can significantly enhance mixing by increasing gradients, and can communicate properties across regions that are not actively mixed by wind. Hence it is of interest to resolve and mechanistically understand the vertical motion generated at submesoscales. In a previous modeling study we found that the vertical advective supply of phytoplankton nutrients to the upper ocean was enhanced several fold when the model resolution was increased from 20 km to 10 km (Mahadevan and Archer, 2000) suggesting that frontal excursions of the order of the internal Rossby radius must be resolved in order to capture the vertical fluxes correctly. Consequently, a modeling study by Lévy et al. (2001) found that vertical nutrient supply is enhanced when the horizontal grid resolution in a Primitive equation model is increased from 6 km to 2 km. This suggested that frontal upwelling occurred on scales finer than the internal Rossby radius, but it was unclear as to how much further the grid resolution needed to be increased in order to capture the vertical motions accurately.

The objective of this numerical modeling study is to examine vertical motion at fronts at finer scales than was previously feasible. We examine $O(1\text{ km})$ motions in this regime with a three-dimensional (3-D), fully non-hydrostatic, free-surface ocean model. The numerical experiments are set within a periodic channel that is initialized with an unstable density front that evolves into an active frontal flow field. We elucidate distinctions between the broad, mesoscale up- and down-welling associated with frontal meanders and eddies, and the elongated, submesoscale patches of vertical motion that develop closer to the surface and have strong directional asymmetry. Several numerical experiments are performed to assess the characteristics of the submesoscale motions. We perform simulations with and without wind forcing in order to determine if the features result from forced or spontaneous instabilities. Secondly, we test the robustness of the submesoscale features in the model by varying the horizontal grid resolution between 1 km and 0.25 km. Thirdly, we attempt to identify the role of nonhydrostatic (NH) effects at submeso scales. This is achieved by comparing solutions from

the NH model and a hydrostatic (HY) version of the same model. Scaling arguments suggest that NH effects are relevant when the aspect (depth to length) ratio δ , and Rossby number Ro , of the flow are $O(1)$ or less. Thus, NH effects are thought to be inconsequential at meso and larger scales and NH ocean models are used almost exclusively to study small-scale, three-dimensional phenomena such as convection and internal wave breaking (Brugge et al., 1991; Jones and Marshall, 1993; Sander et al., 1995; Marshall et al., 1997; Kämpf and Backhaus, 1998; Winters et al., 2000; Dietrich and Lin, 2002; Haine and Williams, 2002; Chao and Shaw, 2002; Legg and Adcroft, 2003). Less, however, is known about the role of NH effects on vertical accelerations at the intermediate (submeso) scale, and assessing these is a central part of this work. A follow on paper examines the mechanisms contributing to submesoscale up- and down-welling in the model (Mahadevan and Tandon, 2006). Further work is needed, however, to fully understand the factors that control the intensity of the vertical velocities at fronts, the length scales of the submesoscale features, and their cumulative effect on tracer transport.

In what follows, we briefly describe the NH model (Section 2.1), how it differs from the HY model (Section 2.2), inherent differences in the NH and HY balanced states (Section 2.3) and inertial oscillations (Section 2.4). These differences are relevant for assessing the role of NH effects and comparing HY and NH model solutions. The reader who is not interested in the NH aspects of the work, may skip this part. In Section 3, we describe the numerical experiments, including the solution procedure that enables comparison of the HY and NH model solutions (Section 3.1) and the model set up (Section 3.2). In Section 4, we compare the numerical model solutions from the HY and NH models at varying grid resolutions in the absence of wind (Section 4.1) and with wind forcing (Section 4.2). We describe the mesoscale frontal meanders and the submesoscale secondary circulation in the wind-forced model runs. Section 5 provides a discussion and is followed by some concluding remarks.

2. Modeling

2.1. Nonhydrostatic model

The model is an extension of the three-dimensional, nonhydrostatic, free-surface model described in Mahadevan et al. (1996b). The non-dimensional form of the model equations in a local coordinate system x (eastward), y (northward), z (upward) on the surface of the earth, neglecting the curvature of the earth's surface, is written as

$$D_t \rho = F^\rho, \quad (1)$$

$$D_t u + Ro^{-1}(p_x + \gamma q_x - fv + Ro \delta bw) = F^x, \quad (2)$$

$$D_t v + Ro^{-1}(p_y + \gamma q_y + fu) = F^y, \quad (3)$$

$$D_t w + Ro^{-2} \delta^{-1} \left(\frac{\gamma}{\delta} q_z - bu \right) = F^z, \quad (4)$$

$$u_x + v_y + Ro w_z = 0, \quad (5)$$

where the non-dimensional material derivative operator $D_t \equiv \partial_t + u \partial_x + v \partial_y + Ro w \partial_z$. Here, u, v, w denote the velocity components in the x, y, z coordinate system. The important non-dimensional parameters in (1)–(5) are γ , the ratio of NH to HY pressure variations, the aspect ratio $\delta \equiv D/L$, and the Rossby number $Ro \equiv U/\Omega L$, where L and D are the characteristic length scales in the horizontal and vertical directions, U and W are the corresponding characteristic velocities, and Ω is the angular velocity of rotation of the earth. Time, t , is non-dimensionalized by the horizontal advection time scale L/U . Scaling the vorticity equation suggests that $W = Ro \delta U$ (Mahadevan et al., 1996a). This scaling is consistent with Molemaker et al. (2005) and it is worth noting that it differs from the traditional choice $W = \delta U$. The components of the Coriolis acceleration in the x, y, z coordinate directions are $-fv + bw, fu, bu$, where $f \equiv 2 \sin \phi$ and $b \equiv 2 \cos \phi$ have been normalized by Ω . Eq. (1) describes the advection of potential density ρ ; in its place one may use equations for salinity and temperature, from which ρ can be inferred. The right hand side terms F^ρ, F^x, F^y, F^z are used to denote mixing and forcing. For example, $F^x = (UL)^{-1}(\partial_x(K_H \partial_x u) + \partial_y(K_H \partial_y u) + \delta^{-2} \partial_z(K_V \partial_z u))$ may be used to account for viscous dissipation, where K_H and K_V are horizontal and vertical eddy viscosities. The fluid pressure is resolved

into its HY component p , and its NH component q . The HY pressure p , by definition, satisfies $p_z + \rho g = 0$, where g is the acceleration due to gravity. This relation is used to eliminate p from the vertical momentum equation (4). The value of p at any point in the fluid can be calculated by vertically integrating the HY relation from a given location z to the height of the free-surface h , which is obtained by solving the vertically integrated form of (5), namely,

$$h_t + \partial_x \int_z^h u \, dz + \partial_y \int_z^h v \, dz = 0. \quad (6)$$

From Eq. (4), it can be seen that γ must be the same order as δ in order for the two largest terms in the vertical momentum equation to be in balance (Mahadevan et al., 1996a). Thus, the ratio of the NH to HY pressure gradient γ , which appears in (2) and (3), is of the order of the aspect ratio δ , i.e., $\gamma = \delta$. The parameters δ and Ro are typically $\ll 1$ for meso (10–100 km) and larger length scales in the ocean, but approach 1 as the horizontal length scale is reduced (to a kilometer or less). As δ approaches 1 (i.e., γ approaches 1) the NH pressure gradient becomes comparable in size to the HY pressure gradient in the horizontal. Typically Ro increases simultaneously and the coefficient $1/(Ro^2\delta)$ in (4) ceases to be much larger than 1. When this occurs, a significant vertical acceleration can be induced by the imbalance between the nonhydrostatic vertical pressure gradient and the vertical component of the Coriolis acceleration. The coefficient $1/(Ro^2\delta)$ in (4) is thus a measure of the degree of HY balance. In Mahadevan et al. (1996a), we reduced the coefficient $1/(Ro^2\delta)$ by a few orders of magnitude based on a scaling argument by Browning et al. (1990), which showed that the error made by this approximation is negligible for meso and larger scale flows. Here, however, we leave the coefficient $1/(Ro^2\delta)$ unmodified to retain the “exact” form of the NH equations, which is appropriate in situations where Ro and δ approach 1. Density stratification is not considered in this scaling. However, with stratification, the parameter F/N (where F is the dimensional Coriolis parameter and N the buoyancy frequency) defines the aspect ratio; it is equivalent to δ for a Burger number ($\equiv ND/FL$) of $O(1)$.

2.2. How the nonhydrostatic and hydrostatic models differ

In the HY model, also known as the Primitive equation model, the pressure is ascribed entirely to the weight of overlying fluid and the vertical momentum equation is reduced to an expression for hydrostatic balance. Vertical velocity is diagnosed from the constraint that the fluid, assumed incompressible, is divergence free. The NH model differs from its HY counterpart (viz. the Primitive equations) due to the inclusion of (i) the NH pressure gradient, and (ii) the Coriolis acceleration terms bu and bv that contain the component of the earth’s angular velocity $\Omega \cos(\text{latitude})$, in a direction tangential to the surface of the earth. The Coriolis acceleration terms containing b are customarily neglected in the Primitive equations, but bu is a dominant term in the NH vertical momentum equation (4), as it is the only term balancing q_z . This is apparent once the hydrostatic balance is subtracted out. The imbalance between bu and q_z gives rise to vertical acceleration. However, the NH pressure q , is constrained so that the resulting velocity field is divergence free. Setting $\gamma = 0$ and $b = 0$ in Eqs.(1)–(5) converts the model from NH to HY.

2.3. Balanced state

The balanced state resulting in the absence of inertial motion is obtained by neglecting the inertial terms that are $\leq O(Ro)$ in (2)–(4). For the NH model, it is expressed in non-dimensional variables as

$$fv_g = p_x + \gamma q_x - Ro \, bw, \quad -fu_g = p_y + \gamma q_y, \quad bu_g = \frac{\gamma}{\delta} q_z. \quad (7)$$

The subscript g on the velocities is used in analogy with geostrophic balance for the HY case, which is obtained by setting $\gamma = 0$ and $b = 0$ in the above equations. In the NH model, b is non-zero and $\gamma = \delta$. A balanced state can be achieved with $w = 0$. But, if u is non-zero, q_z must be non-zero implying that NH pressure gradients will necessarily exist. If p_y , and consequently u_g , is uniform in x, y over the domain, then q_z is uniform in x, y and $q = q(z)$. Then q_x and q_y are 0 and u_g, v_g are the same as in the HY case. However, more commonly, u_g and p_y vary with x, y . In this case, $q = q(x, y, z)$ and q_x, q_y contribute to u_g, v_g . For example,

in the case of a front, a localized pressure gradient is developed in the across-front (y) direction such that p_y and u_g are large at the front. In this case, q_z is non-zero and also varies in y since u_g varies in y , i.e., $u_g = u_g(y, z)$, $q = q(y, z)$.

The geostrophic velocities u_g, v_g are easily computed given the HY pressure gradients p_x, p_y . In the NH case, this is done iteratively so as to involve q . First, we compute u_g, v_g while neglecting the NH pressure gradients q_x, q_y . Next, we compute q_z based on u_g and the boundary condition $q = 0$ at the free-surface. Finally, we need to recompute u_g, v_g incorporating q_x, q_y . The process of computing q based on u_g and then updating u_g, v_g based on q is repeated a few times to attain a converged solution. Fig. 1 shows the balanced HY and NH velocities u_g, v_g for an idealized front. The situation shown is a cross-section across a rectangular channel with a vertical front separating waters of two different densities. The free-surface is elevated on the side with the lighter water. The prescribed density field and free-surface elevation determine the HY pressure gradients. Here $p_x = 0$ and p_y is non-zero. The geostrophic velocity u_g is a jet directed out of the paper. But in the NH solution, the jet is tilted in the vertical with respect to the front due to the NH pressure gradient. In the vertical, u_g is balanced by the vertical component of the NH pressure gradient; its horizontal component modifies the horizontal velocity u_g and makes it asymmetric. The flow is speeded up by q_y on one side of the front and slowed down on the other. This in turn makes q_z asymmetric and effectively tilts the jet making it non-coincident with the density front. The barotropic pressure gradient in this example (Fig. 1) is exaggerated to generate a jet that persists with depth so as to highlight the difference between the NH and NH balanced states.

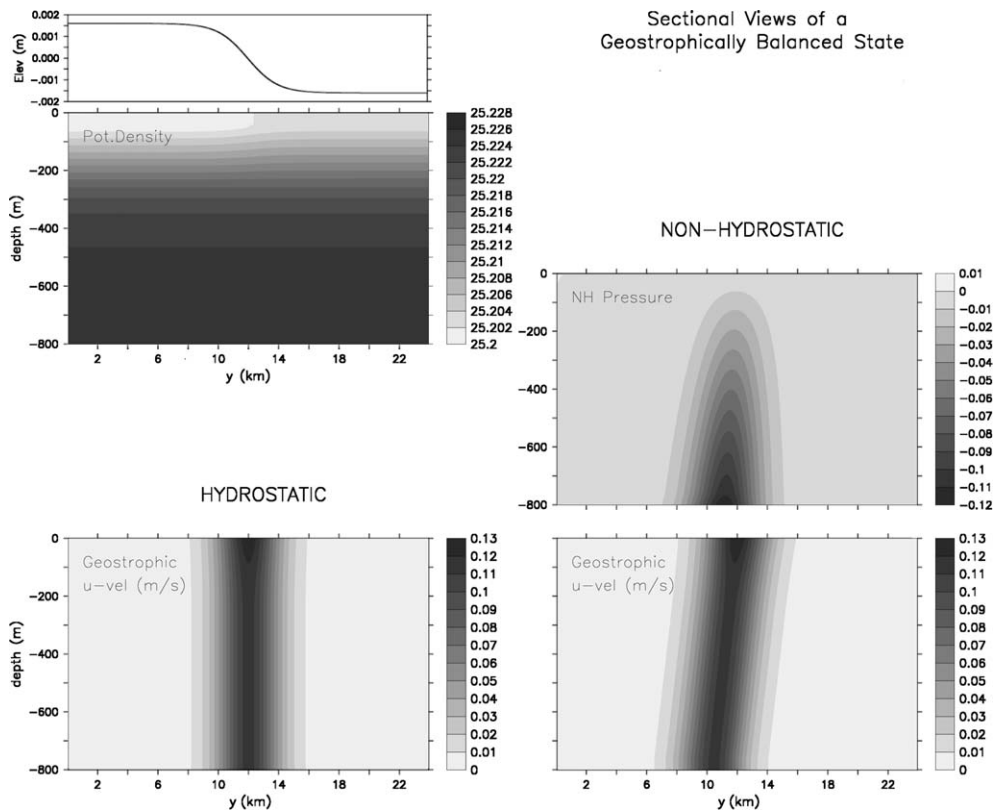


Fig. 1. A vertical cross-section through a rectangular channel-like domain showing an idealized front and the corresponding balanced velocities. The top left figures show the prescribed free-surface elevation and density field. There are no variations in the direction normal to the paper. The baroclinic pressure gradient is restricted to the upper 100 m, while a free-surface profile that generates a rather deep barotropic jet is chosen to illustrate the differences between the hydrostatic and nonhydrostatic flow more clearly. The lower left figure shows the geostrophically balanced velocity field in response to the prescribed free-surface and density field for the hydrostatic equations. The lower right figures show the corresponding velocity for the nonhydrostatic case along with the nonhydrostatic pressure distribution.

2.4. Inertial oscillations in the nonhydrostatic model

Inertial oscillations, a common feature of the oceans, arise in response to disequilibrium from geostrophy. These can sometimes be problematic in models, as the associated velocities are generally not of interest, but can form a significant part of the solution. Inertial oscillations differ between the HY and NH models, and this difference must be kept in mind when comparing model solutions. In the HY model, inertial oscillations consist of a horizontal velocity vector that rotates at the inertial frequency f generating elliptical fluid trajectories in the horizontal plane. In the NH model, they contain an additional vertical velocity component that arises from the imbalance between the terms q_z and bu in the vertical momentum Eq. (4). This tilts the elliptical fluid trajectories out of the horizontal plane. A more detailed analysis of NH inertial oscillations is provided in Kasahara (2003b), Kasahara (2003a). If the inertial oscillations are to be filtered, a different filter needs to be designed for each of the models. In the numerical experiments, we initialize the model with a geostrophically balanced state to minimize the inertial oscillations in the system and ensure that they do not form a significant part of the solution. We do not use any filtering. The balanced state used for initialization is particular to the HY and NH models.

3. Numerical experiments

3.1. Solution procedure

A numerical solution procedure is developed to run the NH and HY versions of the model within a numerically consistent framework. This puts us in a position to make systematic comparisons between NH and HY solutions. The numerical solution of the NH model described by Eqs. (1)–(6) is achieved in two stages. The first is to find the HY pressure distribution and HY velocity field; the second involves computing the NH pressure distribution that results in a final 3-D velocity field that is divergence-free. The solution procedure consists of (1) calculating the advective contribution to the velocities and tracers, (2) solving a two-dimensional elliptic equation for the free-surface elevation h , at a new time based on the semi-implicit discretization of the momentum and free-surface equations, (3) updating the horizontal velocities with the updated HY pressure gradient, but original NH pressure gradient and Coriolis terms at the previous time, (4) computing the correction to the NH pressure field under the constraint that the final velocities that are updated with the corrected pressure gradients be divergence free, and (5) updating the velocities. Most aspects of this procedure are described in Mahadevan et al. (1996b), but to maintain consistency between NH and HY models, we find it necessary that the NH pressure gradients appear in the formulation of the free-surface equation at the first stage, and that the second stage entails computing the correction the NH pressure field that updates it to the new time level. Finally, the velocities are updated to the new time.

The NH model can be run in HY mode by merely zeroing out certain parameters, while leaving all other aspects of the model unchanged, as suggested in Marshall et al. (1997). In the above model, setting $\gamma = 0$ and $b = 0$ results in the hydrostatic (Primitive) equations. When γ is set to 0, there is no NH pressure contribution to the momentum equations. In this case, the solution of the NH pressure equation serves to evaluate a potential field q , which, when used in (4) to update the vertical velocity w , results in a velocity field that is divergence free. Since γ is the same size as δ in the NH model, a smaller value of δ implies a lesser contribution of NH effects. In the HY model results presented here, the $\cos(\text{latitude})$ term b is set to zero, as is generally the case in HY models. However, the $\cos(\text{latitude})$ terms bu and bw may be retained independently of the NH pressure effects, particularly when the model region is situated in the low latitudes.

The NH model, in comparison to its HY counterpart, requires the additional computational effort of finding the three-dimensional NH pressure field subject to the incompressibility constraint. However, by exploiting the skewness of the system in formulating the pressure equation, and by using a multigrid solver (Mahadevan et al., 1996b), we are able to attain a computational performance speed for the NH model that is two-thirds the speed of the corresponding HY model. Furthermore, we believe that the NH model is more amenable to the implementation of open boundary conditions, because it is mathematically well-posed in domains with open boundaries even without the viscous terms (Mahadevan and Archer, 1998).

3.2. Model set up and experiments

3.2.1. Domain

We perform several NH and HY model simulations of a baroclinically unstable upper-ocean front set within a west-to-east (W–E) periodic channel. The model domain extends 48 km in the W–E (periodic) direction, 96 km in the south-to-north (S–N) direction, and is centered at a latitude of 25°N. Impermeable, vertical walls form the northern and southern boundaries of the domain and a flat bottom forms the lower boundary at 800 m. The model domain is discretized using uniform, rectilinear grid cells in the plan view and a stretched, boundary-fitted sigma grid in the vertical. The upper layer of grid cells conform to the moving free-surface. A stretched, vertical discretization that varies from 10 m at the surface to 75 m at depth, is used to permit increased resolution toward the surface. Horizontal grid resolutions of 1 km and 0.5 km are used routinely in the experiments, but the vertical resolution is not varied because the model solution is much less sensitive to refinement in the vertical. The time step of integration is 400 s.

3.2.2. Initialization

The domain is initialized with a sharp lateral south-to-north (S–N) density gradient in the upper layers, such that the southern half of the domain has lighter water as shown in Fig. 2. This front is representative of the deep, semi-permanent fronts that are observed in the ocean (Rudnick, 1996) and extends to a depth of 250 m. The vertical stratification is prescribed from a spline fit to an observed open ocean profile. The pycnocline, which is characterized by an approximate buoyancy frequency $N = 0.7 \times 10^{-2} \text{ s}^{-1}$, extends to about 250 m. It overlies a weakly stratified region and a nearly homogeneous deeper layer. A S–N density variation $\Delta\rho$, is then superimposed on this vertical stratification. In the upper 50 m $\Delta\rho = 0.3 \text{ kg m}^{-3}$, between 50 and 250 m $\Delta\rho = 0.3(250 - z)/200 \text{ kg m}^{-3}$, where z is the depth in m, and below 250 m, there is no horizontal density variation. The density variation in the S–N direction is distributed according to $(\pm\Delta\rho/2)(1 - \exp(-y_c/2))/(1 + \exp(-y_c/2))$, where y_c is the distance in km from the channel center (northward is positive), and the \pm signs are used according as y_c is positive or negative. The sea surface elevation is varied correspondingly over the same frontal region by 3.2 cm, being higher in the southern region. Associated with the S–N density front is a west-to-east (W–E) geostrophic jet. The model velocities (and the NH pressure in the NH model) are initialized to satisfy the model's respective NH or HY balanced state as described in Section 2.3. The model is allowed to evolve from this balanced state into a meandering front, generating smaller scale features, when perturbed by wind. We examine the flow fields over the course of the numerical experiments, which run for a period of 50–100 days from initialization. Since the across channel frontal gradients are not restored, the front decays gradually in time.

3.2.3. Wind forcing and mixing

Model runs that are forced with a surface wind stress (τ^x, τ^y) , use the relation $\rho K_V u_z = \tau^x$, $\rho K_V v_z = \tau^y$ at the free-surface. Here K_V represents the vertical eddy viscosity in the model. Since the model domain has solid walls on S–N boundaries, we prescribe only a westerly (W–E) wind stress. A sustained easterly wind stress would upwell denser water at the southern wall, annihilating the S–N density front. Hence, we use either a constant westerly wind stress $\tau^x = 0.025 \text{ N m}^{-2}$, or a sinusoidally varying wind stress τ^x with an amplitude of 0.025 or 0.075 N m^{-2} and a period of 10 days. Bottom friction is prescribed using a linear drag ru , where the frictional parameter $r = 5 \times 10^{-4} \text{ s}^{-1}$. Since the qualitative character of the submesoscale velocities is similar in the various experiments, we present only the experiments with a uniform, time-invariant westerly wind stress. Uniform eddy viscosities, $K_V = 10^{-5} \text{ m}^2 \text{ s}^{-1}$ in the vertical and $K_H = 10 \text{ m}^2 \text{ s}^{-1}$ in the horizontal (K_H was doubled in the y direction to contend with the Ekman up- and down-welling jets at the channel walls) are used for all the model runs. Convective adjustment is performed at each time step when using a constant value of K_V . Experiments are also carried out with a variable mixing coefficient derived from the KPP scheme (Large et al., 1994), but these turn out to be more diffusive and are not presented. Enhanced mixing in the surface mixed layer does not significantly alter the submesoscale character of the flow or change the conclusions drawn from this study, but its implication on fluxes needs to be further investigated (Nagai et al., 2006).

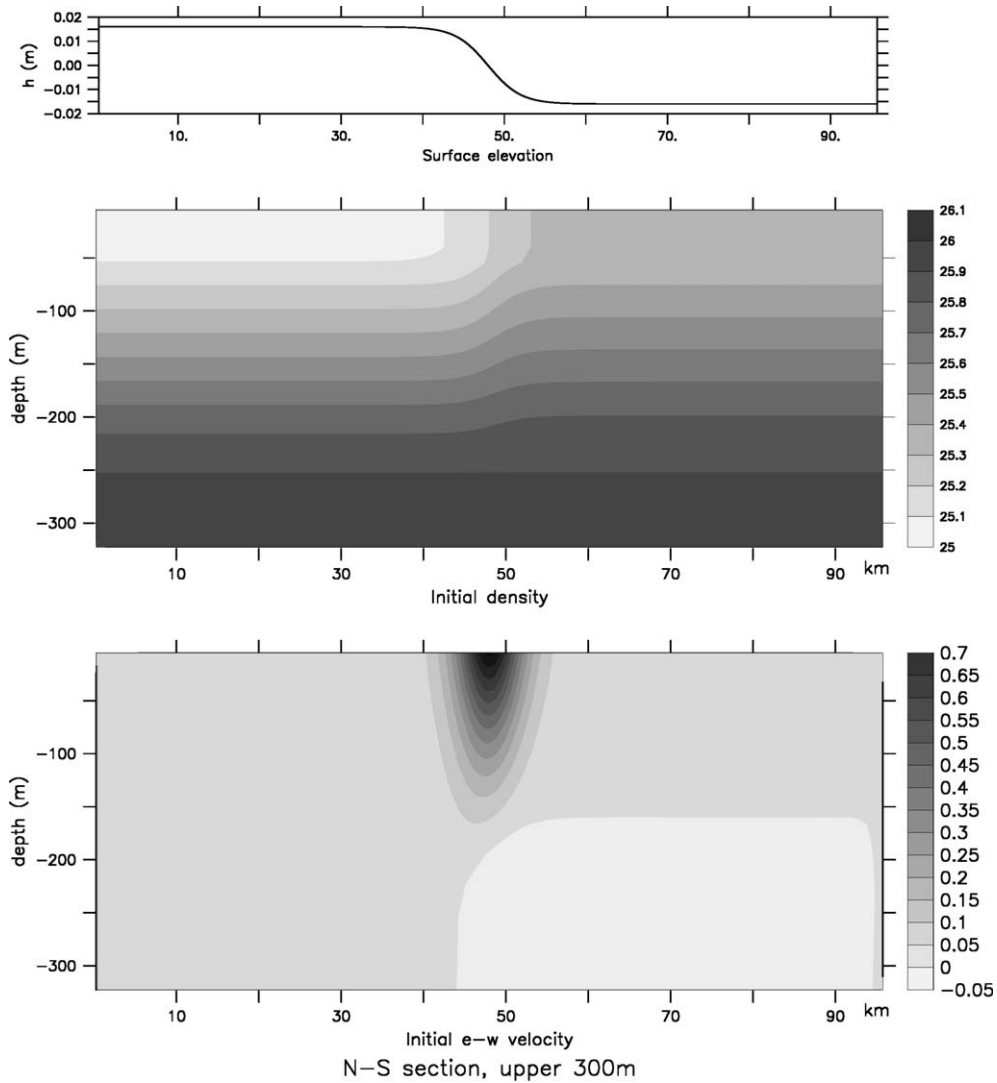


Fig. 2. Across-channel cross section showing the sea surface elevation, potential density and along-channel velocity in the upper 300 m that were used to initialize the model with an upper ocean front.

Some variations of the model configuration described above are also used; these are described where appropriate, along with the corresponding results.

4. Results

The numerical experiments presented here are used to address questions about the the relevance of NH effects at the $O(1 \text{ km})$ scale, the effect of wind on submesoscale motions, and the numerical resolution required for modeling the vertical velocity field at fronts. By comparison of the HY and NH model solutions from several experiments we attempt to assess the role of NH effects on the evolution of the front and the development of meso- and submeso-scale vertical motion. We test whether the frontal features in the model are robust and adequately resolved at a horizontal grid resolution of 0.5–1 km. We also test the sensitivity of the vertical velocity and the size of up-/down-welling regions to grid resolution. In each of the frontal experiments, the model is initialized with a linear W–E front as described. Our experiments are performed with and without

Table 1
A summary of the numerical experiments

Experiment	Forcing, Initialization	Hor grid Resol ^a	HY NH	Salient Findings
Upper ocean front: Flat bottom, W–E periodic channel, 48 km x 96 km. Figs. 3 and 4	Initialized as in Fig. 2. <i>No forcing</i>	1 km	HY	Mesoscale up-/down-welling seen on meander scale. Down-welling is 1.5 times more intense than upwelling. <i>Effect of increased resolution:</i> Magnitude of w increases by a factor of 1.5. Vertical velocities confined to narrower regions <i>NH effects:</i> Phase of instability and instantaneous solution differ. No other categorical differences identified.
		1 km	NH	
		0.5 km	HY	
		0.5 km	NH	
Same as above Figs. 5–8	Initialized as in Fig. 2. <i>Wind-forced</i> Constant westerly stress of 0.025 N/m ²	1 km	HY	Intense submesoscale vertical velocities (~100m/day) in upper 50m overlies weaker (~10m/day) mesoscale up-/down-welling at 50–100 m depth. Down-welling ~1.5 times more intense than upwelling and confined to narrow (2km wide) regions. <i>Effect of increased resolution:</i> Down-welling intensifies by a factor of 2, upward velocities change marginally. <i>NH effects:</i> Instantaneous NH and HY solutions differ. Fluxes (averaged upward w) are similar in both.
		1 km	NH	
		0.5 km	HY	
		0.5 km	NH	
		0.25 km	NH	
Same as above Not shown	Sinusoidally varying wind. Amplitude 0.025 N/m ² , Period =10 d.	0.5 km	NH	Submesoscale vertical velocities weaken as wind drops.
Front over shelfbreak topography: W–E periodic channel, 48 km x 96 km, varying topography – shelf in south, deeper in north Fig. 9	Surface-to-bottom front at shelf break. Weak vertical stratification. <i>Wind-forced</i> Constant westerly stress of 0.025 N/m ²	1 km	HY	Intense submesoscale vertical velocities penetrating deeper due to lack of vertical stratification. Downwelling more intense than upwelling by a factor of 2. <i>Effect of increased resolution:</i> Stronger lateral density gradients are maintained over time. <i>NH effects:</i> Not discernible.
		1 km	HY	
		0.5 km	NH	
		0.5 km	NH	

wind forcing to determine the role of wind in the generation of submesoscale structure at fronts. The experiments are summarized in Table 1.

4.1. Unforced case: comparison of HY and NH solutions at varying grid resolutions

The initially straight front becomes baroclinically unstable, forming meanders of initial wavelength 10–15 km. These progressively coalesce and grow, resulting ultimately in one large meander that fills the domain (Fig. 3). With numerically consistent versions of the NH and HY models, we compare their respective solutions using horizontal grid resolutions of 1 km and 0.5 km. The various model runs evolve differently causing the solutions to diverge with time. The frontal meander in the NH and HY models evolves at slightly (~5%) different rates, indicating a different growth rate for baroclinic instability in the NH and HY case (Molemaker et al., 2005). Correspondingly, the fronts also relax the upper ocean to horizontal stratification at slightly different rates. Associated with the mesoscale meander, we observe a broad upwelling on the less dense side of the front and a narrower, elongated region of down-welling that is aligned with the frontal isopycnals in the region

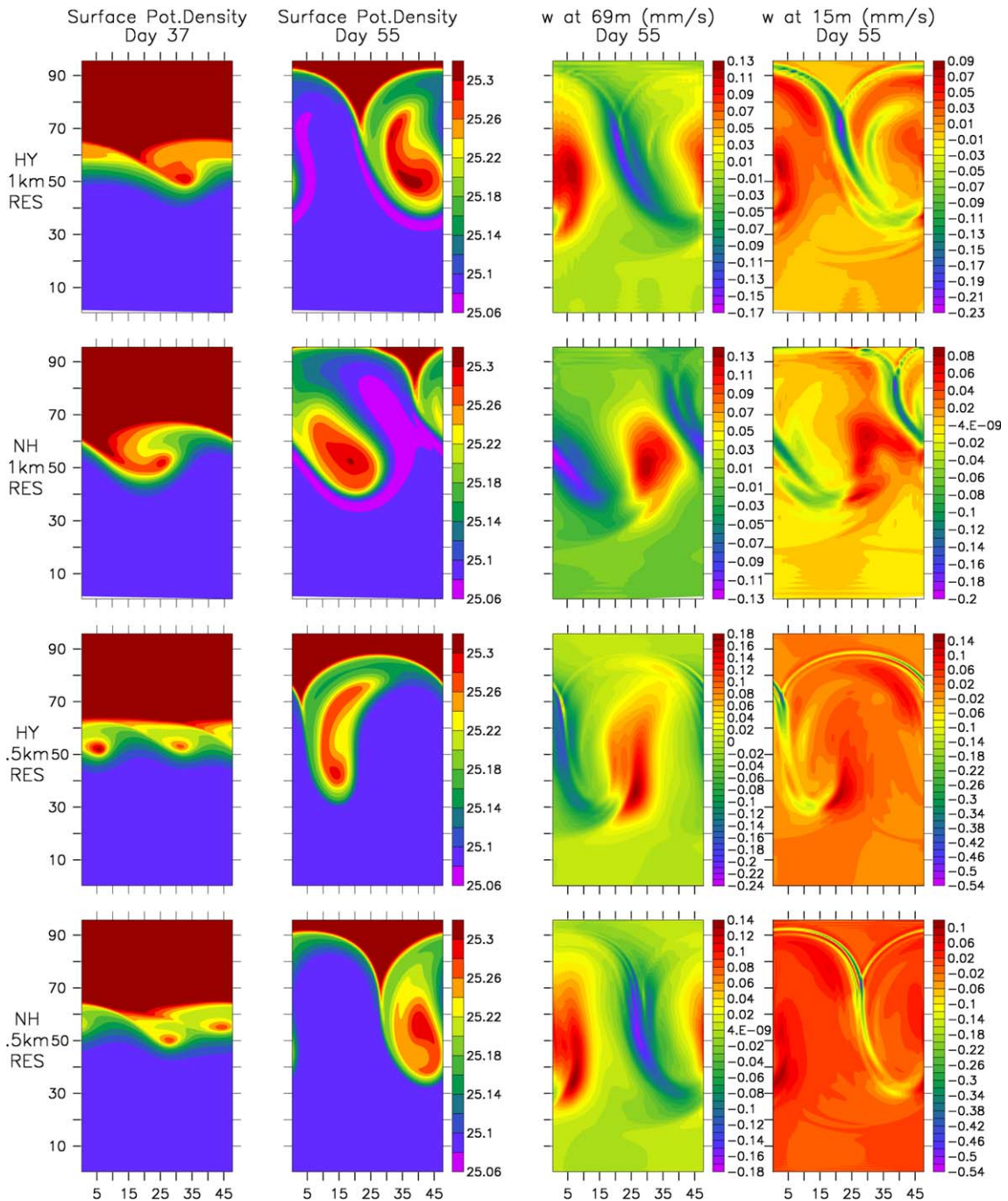


Fig. 3. The surface potential density for a developing frontal meander shown 37 and 55 days after model initialization for the NH and HY models run at 1 km and 0.5 km resolution. The corresponding vertical velocity w , is shown at a depth of 69 m and 15 m on day 55. No wind forcing is used. The growth and propagation of the meander differs in the NH and HY case and at different resolutions, leading to divergent solutions as the simulations progress. The color scales used for w reflect the range of values, which differ at the two resolutions. The density gradients and vertical velocities are more intense at higher resolution. (For interpretation of the references in colour in this figure legend, the reader is referred to the web version of this article.)

where the flow field is strained most rapidly. There is a notable asymmetry in the mesoscale up- and down-welling velocities. When the horizontal model resolution is increased from 1 km to 0.5 km, the

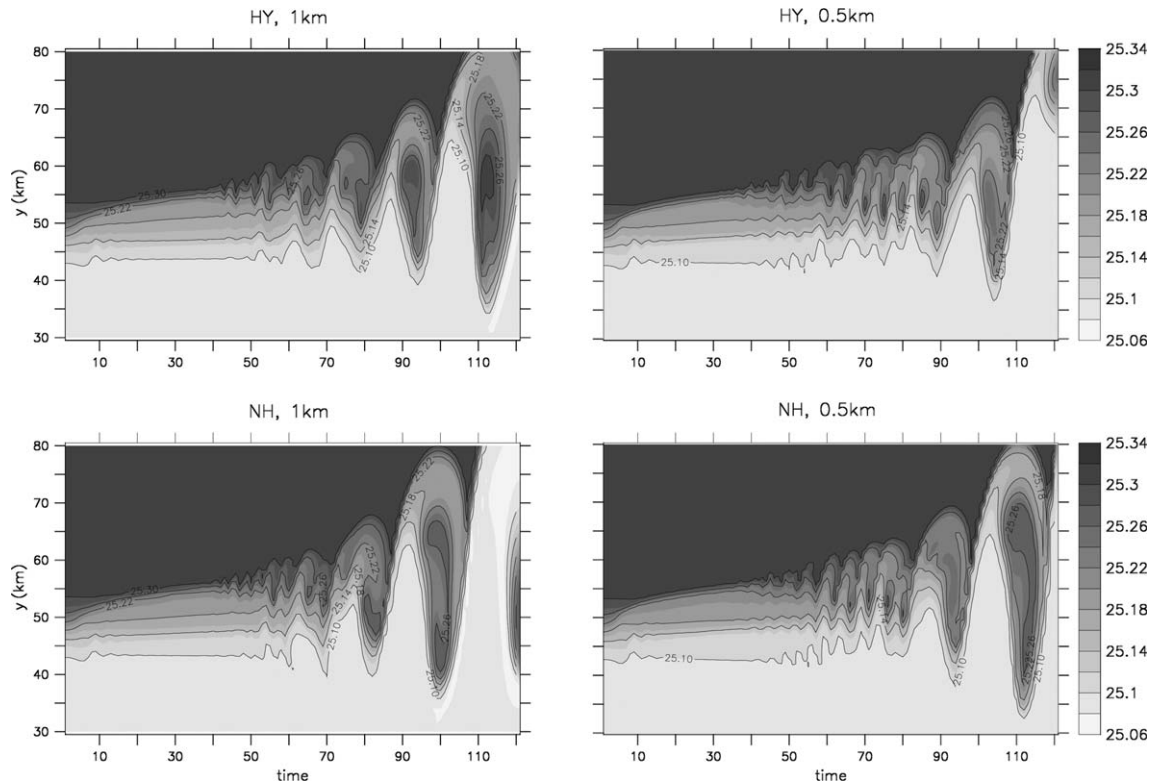


Fig. 4. A Hofmuller plot of the across-front surface potential density shown to evolve in time (indicated in dimensionless units), ranging from 0 to 55 days, for the NH and HY models run at 1 km and 0.5 km grid resolution. No wind forcing is used. The development of baroclinic instability differs slightly in the NH and HY cases and at 1 km and 0.5 km grid resolutions.

frontal gradients are intensified and smaller scale vortices develop and pinch off from the front during its early evolution (Fig. 3 left panels). The frontal meander and eddy that develop are both narrower in shape; the up and down-welling regions are more focused and the vertical velocities are intensified. Fig. 3 shows the initial instability, pinch off of the elongated meander into an eddy, and the vertical velocities that are associated with the mesoscale flow field in the various model runs, HY and NH at 1 km and 0.5 km resolution. The flow is not perturbed by wind, topographic variations, or buoyancy fluxes in this case, and does not exhibit the same degree of submesoscale structure seen in later experiments. Inertial oscillations are not a significant part of the solution. In Fig. 4 we plot the across front density along a section as a function of time. This shows differences in the rate of development of baroclinic instability in the various model runs.

4.2. Wind forced case: submesoscale vertical motion

The mesoscale frontal meander that forms in the unforced case develops a profusion of submesoscale frontal structures when a wind stress is applied at the sea surface. In the model simulations forced by wind (Fig. 5), submesoscale regions of intense up- and down-welling (~ 100 m/day) develop in the near-surface layer (upper 50 m) of the ocean. The intense vertical motion appears in elongated regions that are coincident with the largest rates of strain in the fluid. The down-welling is approximately twice as intense as the upwelling and is confined to much narrower regions, roughly 2 km in width and notably close to the scale that can be resolved by the model. These submesoscale motions are distinct from the mesoscale up- and down-welling (~ 10 m/day) that is most prominent at a depth of 50–100 m and is associated with the meandering of the front.

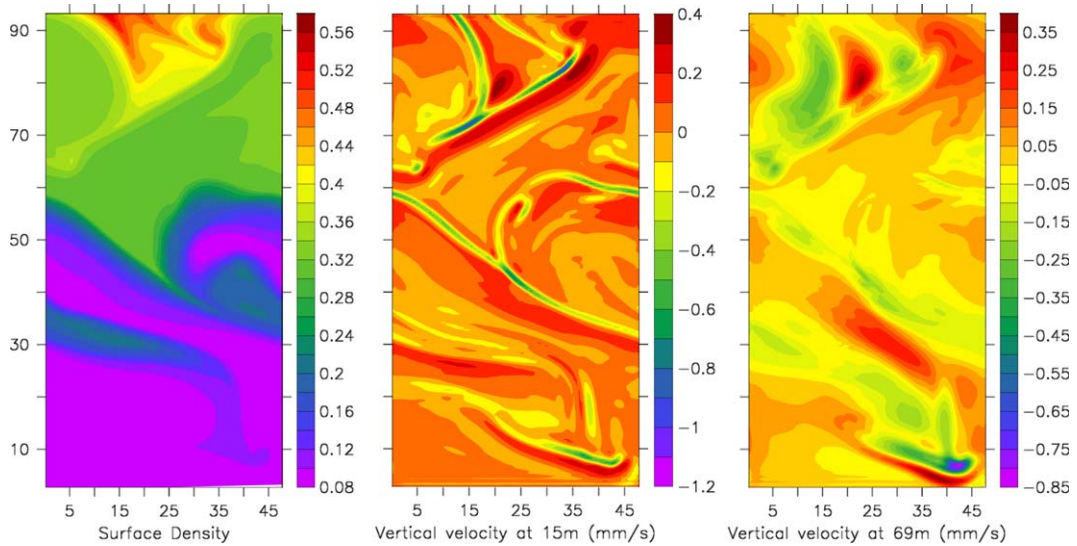


Fig. 5. The surface density and the vertical velocity field (mm/s) shown at 15 m and 69 m depth on day 44 from the 0.5 km grid resolution NH model forced with a constant westerly wind stress of 0.025 N/m^2 . The near-surface (15 m depth) vertical velocity field shows submesoscale structure, while that at 69 m shows mesoscale variability. The submesoscale vertical velocities are considerably more intense than the mesoscale velocities at depth. The color bars show the range of values. (For interpretation of the references in colour in this figure legend, the reader is referred to the web version of this article.)

4.2.1. Differences between mesoscale and submesoscale vertical velocities

As the front evolves, the surface density field develops inflections and cusps (Fig. 5). Submesoscale, vertical circulation cells are formed close to the surface (0–50 m depth) at the tips of cusp-shaped deformations in the outcropping surface isopycnals along the front, where horizontal straining is intense. At a slightly greater depth (50–100 m), we observe up- and down-welling over broader, less elongated patches that are of mesoscale $\sim O(10 \text{ km})$ extent. The asymmetry between upward and downward motion is much less in these structures, than in the near-surface submesoscale phenomena. Thus, the region of mesoscale up- and down-welling, which is typically at a depth of 50–100 m, is overlain by a region of more intense, submesoscale up- and down-welling that is in communication with the air–sea interface.

4.2.2. Comparison of HY and NH solutions at varying grid resolutions

On account of the nonlinear evolution of the flow, the velocities and density distributions from the various model runs, HY and NH, at 1 km and 0.5 km resolution, all differ with time. However, it is difficult to pinpoint characteristic differences between the NH and HY solutions. The differences are significant at the onset of baroclinic instability because the evolution of the instability differs between the HY and NH model. The wavy deformations of surface isopycnals tend to be more angularly oriented in the direction of the mean zonal flow in the NH case. But with time, the field is infused with submesoscale structure and the HY and NH solutions appear statistically similar.

In Fig. 6, we compare a frontal feature from the NH and HY models at various (1 km, 0.5 km) horizontal grid resolutions early in the simulation (day 18.5). This is to ascertain that the submesoscale features are robust and that the down-welling regions do not change width in accordance with the grid size. To determine whether we have resolved the submesoscale features, we further refine the horizontal grid to 0.25 km for a limited duration. The 0.25 km model is initialized with the solution from the 0.5 km model after it has developed frontal character and run for a period of 1–2 days. The near surface, submesoscale vertical velocity field from the 1, 0.5 and 0.25 km resolution model runs, HY and NH, in Fig. 6 are similar in character. We observe a 30% increase in the magnitude of the most intense downward velocities with a doubling of grid resolution, and similarly, a 30% increase in down-welling intensity going from NH to HY models at the same resolution. However, this comparison is from snapshot views of a feature that is in slightly different stages of development. The width

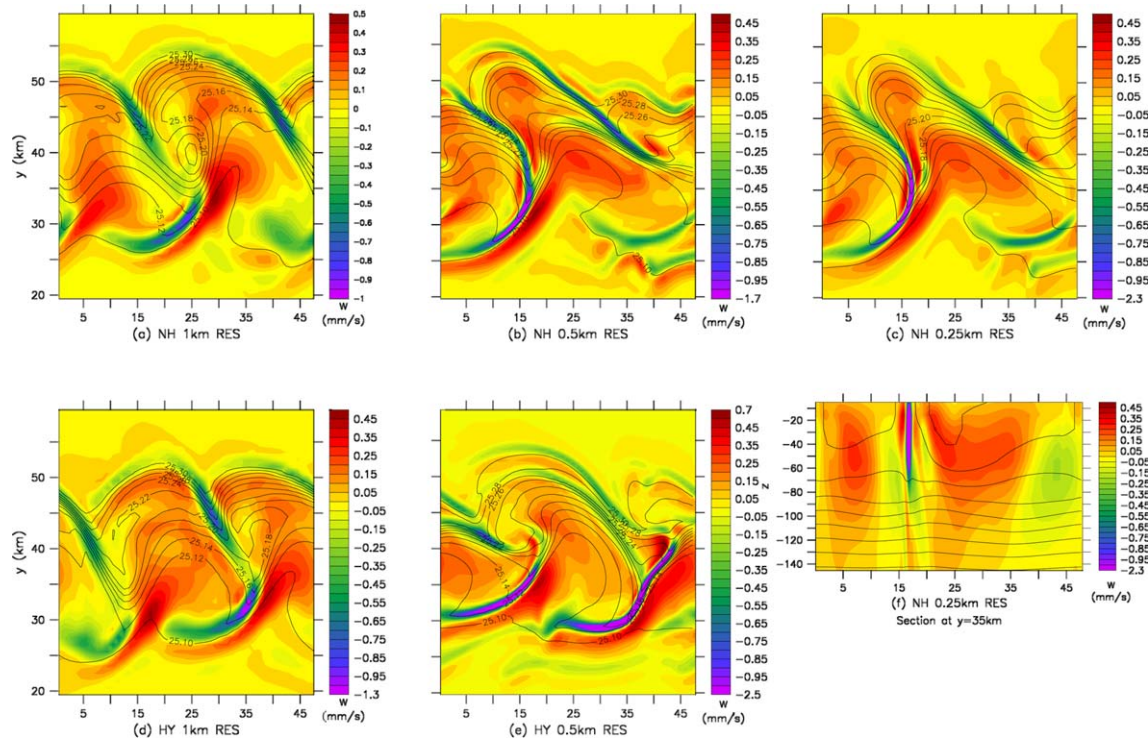


Fig. 6. The near surface vertical velocity at the upper ocean front 18.5 days after model initialization in the NH and HY models at grid resolutions of 1, 0.5 and 0.25 km. The color keys show the ranges of values of w . It is uniformly spaced between -1 mm/s and 0.5 mm/s, but the extreme values chosen to accommodate the full range of w are non-uniformly incremented and vary between the various plots. Strong downwelling can be seen in narrow elongated regions along the front and is more intense in the HY case and at higher model resolutions. The surface potential density is shown with overlying contours. The figure shows only a subregion of the model that was forced with a surface wind stress. The x - and y -axes are labeled in kilometers. The model with a grid resolution of 0.25 km was initialized with the fields from the 0.5 km resolution model on day 17.4, since the highest resolution could not be afforded for the entire simulation. Panel (f) shows the vertical velocities in a vertical section at $y = 35$ km. (For interpretation of the references in colour in this figure legend, the reader is referred to the web version of this article.)

of the down-welling zones is not much different between 0.5 and 0.25 km grid resolution runs, but the finer resolution runs have slightly sharper features and more intense down-welling velocities. Based on comparisons between 1, 0.5 and 0.25 km grid resolution models, we think that the described submesoscale features are adequately resolved with a horizontal grid spacing of 0.5 km. The vertical velocity plotted along a cross-section through the domain (Fig. 6f) shows the near-surface intense down-welling with respect to surrounding mesoscale up- and down-welling.

4.2.3. Statistical comparison of the vertical velocity fields

In order to compare the evolution of the submesoscale vertical velocity field, we plot the near-surface (15 m depth) vertical velocity along an across-front transect over time for the HY and NH models at grid resolutions of 1 km and 0.5 km (Fig. 7). The time period shown in Fig. 7 extends from day 9.25 to day 22.69 of the simulation and includes the time when the flow looks as shown in Fig. 6. The most intense down-welling velocities increase by a factor of 2 in going from 1 km to 0.5 km resolutions, whereas the magnitude of the most intense upwelling velocities increases only marginally with resolution. It is difficult to find categorical differences between the HY and NH vertical velocities, and the differences generated by increasing model resolution are greater than those generated by including NH effects.

In Fig. 8, we plot the domain-wide minimum, maximum and average vertical velocity at a depth of 69 m from the NH and HY model runs at 1 km and 0.5 km resolution. The region considered excludes a strip along

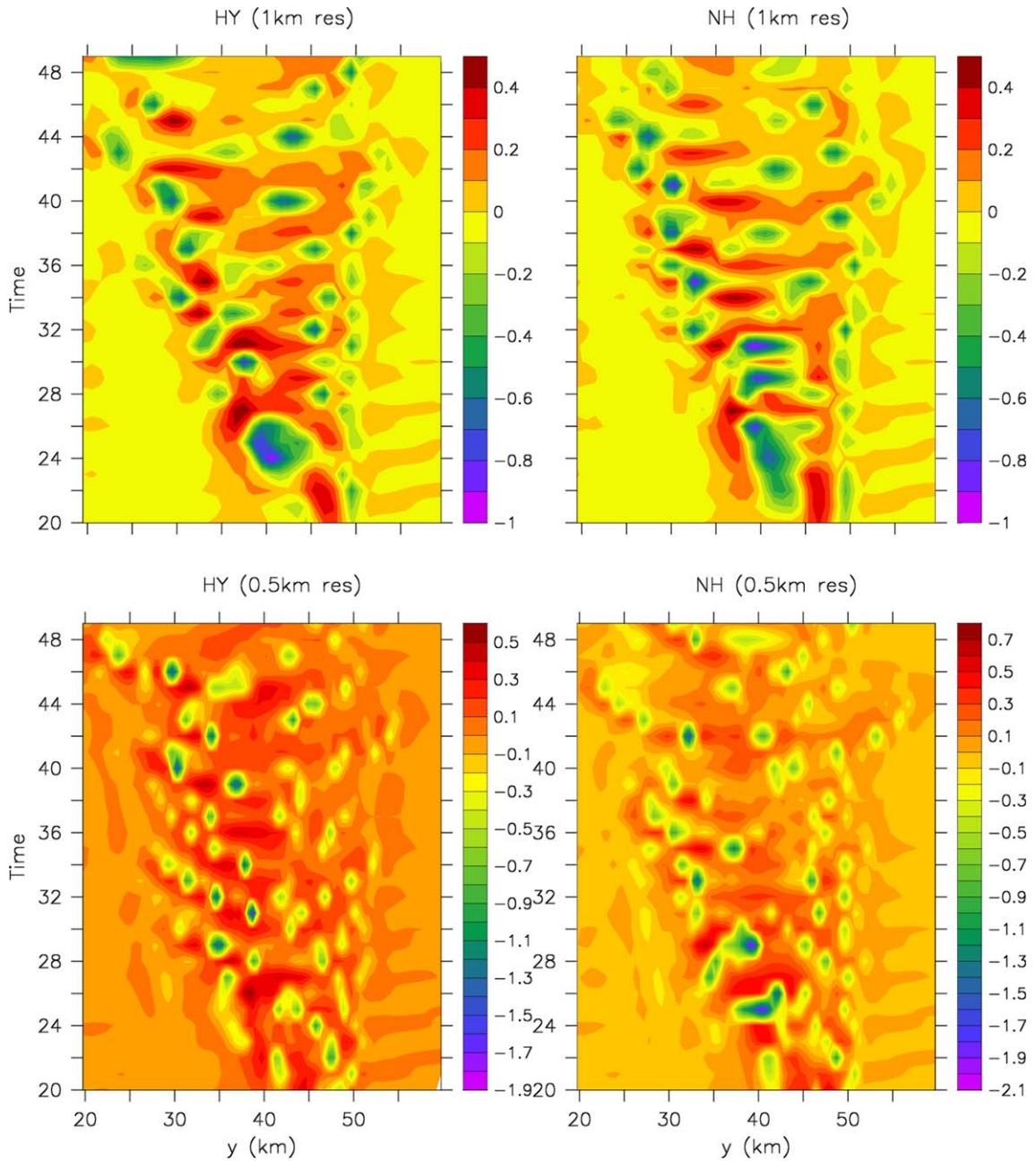


Fig. 7. Hofmuller plot of the near surface (15 m depth) vertical velocity field along an across-front section shown evolving in time (indicated in dimensionless units), ranging from day 9 to 23, for the HY and NH, 1 km and 0.5 km model runs. The color bars indicate the range of values on each field. The statistical character of the vertical velocity field is more affected by model resolution than the inclusion of NH effects. (For interpretation of the references in colour in this figure legend, the reader is referred to the web version of this article.)

the solid northern and southern boundaries of the domain, where upwelling is seen due to boundary effects. The minimum vertical velocity corresponds to the downward maximum velocity at depth of 69 m, which is deeper than the submesoscale maxima. The maximum corresponds to the most intense upwelling at 69 m. The average, corresponds to the average upwelling velocity over the domain at 69 m. The down-welling maxima become more intense with increasing grid resolution, but the upwelling maxima and average are not affected

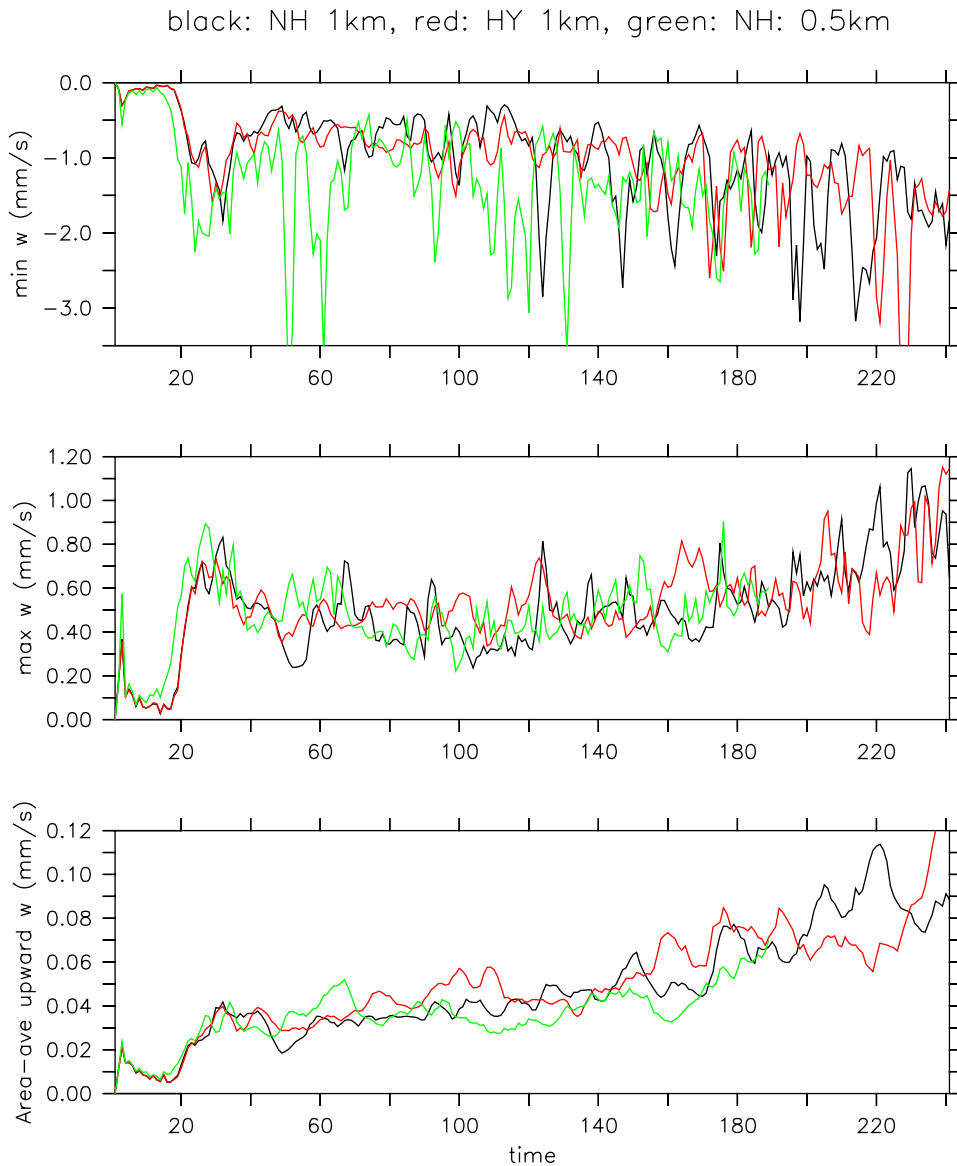


Fig. 8. The maximum, minimum and average upward vertical velocity at 69 m depth plotted against time for the 1 km resolution HY and NH models, and 0.5 km resolution NH model. Down-welling is more intense than upwelling, but it is difficult to pinpoint significant differences between the model runs. Increasing grid resolution increases the most intense downward velocities.

significantly. Even though vertical accelerations are better described by the NH model, it proves difficult to find systematic differences in the vertical velocities from the NH and HY models at the grid resolutions used here.

4.2.4. Varying the wind stress and mixing

In order to test the sensitivity of the observed vertical velocities to wind direction and mixing, we force the upper ocean front with an along-front, sinusoidally varying wind stress. The intensity of the vertical velocities is a function of the magnitude of the wind stress forcing. The submesoscale features weaken but persist during the wind stress reversals. The experiments described above are performed with a constant vertical eddy diffusivity of $10^{-5} \text{ m}^2 \text{ s}^{-1}$ and convective adjustment applied at each time step. Some of these experiments are repeated with the KPP scheme Large et al. (1994) and convective adjustment turned off. But the runs with KPP tend to be more diffusive.

4.2.5. Topographic effects

The submesoscale vertical velocity structure arising at a wind-forced front over shelfbreak topography is shown at 1 and 0.5 km grid resolutions in Fig. 9. These simulations are for a surface-to-bottom front over varying bottom topography that represents the continental shelf and slope. The model domain is a periodic channel as described above, but the bottom topography is varied from extremely shallow (50 m) and shelf-like over the southern half of the domain, to a depth of approximately 200 m at the shelfbreak located

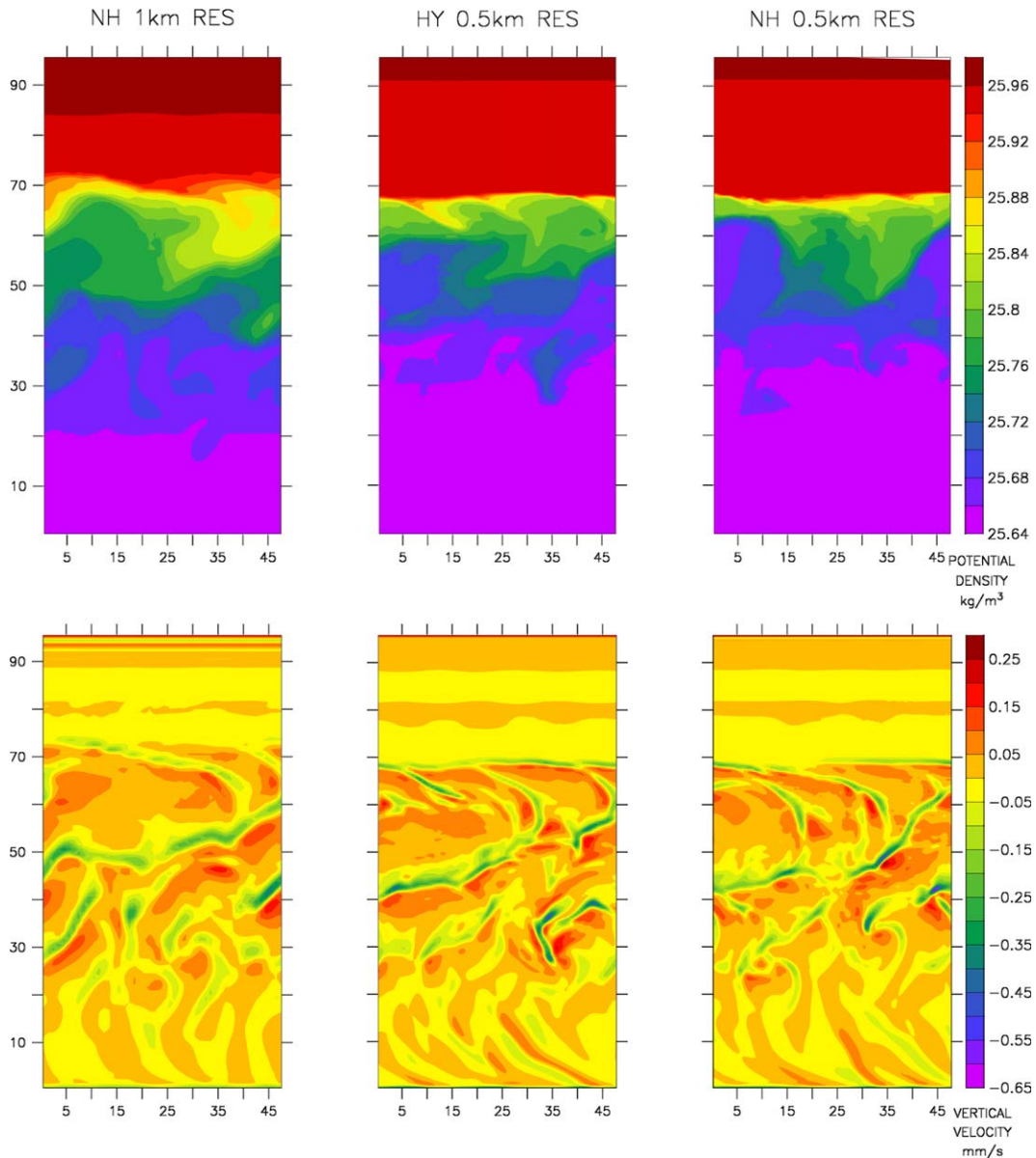


Fig. 9. Comparison of the NH and HY model solutions at horizontal grid resolutions of 0.5 and 1 km. The simulation depicts an unstable front over topography sloping downward from south to north and subject to a uniform wind stress at the surface from west-to-east. The model runs are initialized with a south-to-north density difference of 0.3 kg m^{-3} . The flow is largely from west to east. The domain is periodic in the west–east direction and has solid boundaries to the north and south. The domain dimensions are indicated in kilometers. Shown here are the surface density fields and the vertical velocity just beneath the surface on day 55.5 of the simulation. There is an asymmetry in the strength of the up- and down-ward velocities in these high resolution runs and the color scale is not centered about zero. NH and HY solutions differ, but it is difficult to pinpoint categorical differences. (For interpretation of the references in colour in this figure legend, the reader is referred to the web version of this article.)

mid-channel, beyond which it drops steeply to a depth of 800 m in the northern third of the domain. This topography is fitted with a sigma grid with 24 levels, which conforms to the free surface. The discretization of the hydrostatic pressure in the sigma coordinate system is designed for negligible error (Song, 1998). The model is initialized with lighter water overlying the shallow shelf region and slightly denser water overlying the deeper slope region of the domain. A constant westerly wind stress of 0.025 Nm^{-2} is applied at the surface. The steep gradient in the topography, which is parallel to the front, inhibits growth in the amplitude of the frontal meanders, but the lack of any significant vertical stratification favors the formation of cells with vertical motion. A sharp and fairly straight density front is seen shoreward of the shelfbreak, but the vertical velocities are not most intense at this location where the density gradients are strongest. More intense vertical velocities are seen over the shallower part of the domain where the front is more dispersed and the isopycnals convoluted. The shallow topography does not inhibit the formation of intense near-surface vertical velocities. Even over shallow topography, down-ward velocities are more intense than upward, and down-welling filaments are 1–2 km in width. Both the 1 and 0.5 km resolution model runs develop submesoscale structure, but in the 0.5 km model, the up- and down-welling cells appear better resolved and the front is confined to a narrower region. Characteristic differences between the HY and NH solutions are not discernible at a horizontal grid resolution of 1 km.

5. Discussion

The results from these numerical experiments provide a descriptive picture of submesoscale, frontal processes and the vertical circulation associated with them. Submesoscale features can play a significant role in the transfer of properties, tracers and energy between the surface ocean and upper pycnocline. They bridge the gap between the small scale three-dimensional processes in the upper mixed layer and mesoscale processes in the upper pycnocline, and serve to convey energy from the largely non-dissipative mesoscale to the scale at which dissipation can occur (Molemaker et al., 2005). Many questions about the underlying mechanisms and the conditions for the existence of such motions need to be further addressed. It has been proposed that ageostrophic baroclinic instabilities (Molemaker et al., 2005; McWilliams et al., 2004) and mixed layer instabilities (Fox-Kemper et al., 2006) can generate submesoscale motion and it needs to be ascertained whether the motions that we observe, fit the character of either of these mechanisms. Alternatively, it is feasible that we are observing frontal up- and down-welling at submesoscales.

Though we have a model framework that enables the systematic comparison of NH and HY model solutions, we find it difficult to draw definitive conclusions about role of NH effects. While the early evolution of the HY and NH solutions differs, particularly in the higher resolution model runs, it is difficult to gauge the cumulative contribution of NH effects. One reason is that the models are highly nonlinear, and hence we need to find measures of the statistical differences in the solutions. A limitation in resolving NH behavior is that we need to model a large enough domain to entertain the kind of features that are developed in the ocean, and yet have a resolution that is fine enough to generate features in which the aspect ratio begins to approach $O(1)$. An additional difficulty is that as we approach the grid resolution at which NH effects might be relevant, the HY model becomes less robust and breaks down in some situations. We conjecture that this is because convective, as well as ageostrophic instabilities (c.f. Fig. 2 Molemaker et al., 2005) attain their maximum growth rates at higher wave numbers in the HY, as compared to NH, mode and this may result in unphysically large, grid-scale vertical instabilities in the numerical HY model.

A further question is whether the submesoscale features cumulatively affect vertical fluxes and the large scale flow field. This is difficult to ascertain within the present model set up which has the limitation of solid S–N walls and periodic W–E boundaries, but nonetheless, provides a simple way to generate a frontal flow field. Cumulative tracer fluxes may be used to infer the integrative effect of the vertical motion. However, the advective flux of a tracer in a particular direction, depends both on the fluid velocity and the gradient of the tracer acting in that direction. Hence the efficiency of vertical tracer exchange depends not only on the strength of the up- and down-welling and its locality in space and time, but also on the factors that maintain the vertical gradient of the tracer. These factors include: the horizontal velocity field, which is responsible for dispersing the tracer, the rate at which the tracer might be removed or added, and the evolution of the up- or down-welling location with respect to the tracer and velocity distribution.

In our experiments, we use a surface wind stress to perturb the flow. Submesoscale structure is seen to develop even with wind stresses that are weak or temporally varying in orientation, and over varying bottom topography. However, further work is required to ascertain the dependence of the variability in the submesoscale structure on the wind forcing. Since the oceans are continually forced by wind, it is probable that the submesoscale structures described here, are ubiquitous to the oceans. These motions may be a means by which wind energy is conveyed from the surface layer to the subsurface ocean.

Mixing in the upper ocean, undoubtedly affects the transfer of properties from surface to depth. Vertical mixing can enhance the ageostrophic secondary circulation and the vertical flux of properties at ocean fronts (Nagai et al., 2006). In our numerical investigations, we verify that the submesoscale motions appear even when a mixing parameterization (Large et al., 1994) is used. However, we prefer to conduct the experiments with a small and constant vertical diffusivity ($K_V = 10^{-5} \text{ m}^2 \text{ s}^{-1}$) to facilitate the development of ageostrophic instabilities, which occur under certain critical Richardson number conditions (Molemaker et al., 2005), and would be obliterated by the application of a mixing parameterization.

This study provokes several questions that will be addressed through future work. What is the mechanism that underlies the formation of these features? What sets the length scale of the structures described, their distribution in space and time, and the intensity of the vertical velocities? Can we assess their prevalence and find the means by which we may infer their presence in the ocean? The first of these, is addressed in (Mahadevan and Tandon, 2006). Ultimately, we would like to determine the net contribution of submesoscale circulation to the transport of properties and the transfer of energy between the surface ocean and the thermocline.

6. Concluding remarks

In the presence of adequate numerical resolution and wind forcing, the mesoscale meandering structure of an ocean front is overridden by a multitude of submesoscale frontal features in the upper tens of meters. Strong vertical velocities $O(100 \text{ m/day})$ are associated with these features. Down-welling is considerably more intense than upwelling and occurs within narrow, elongated regions that are typically a couple of kilometers in width. Upwelling occurs on larger scales. These motions differ from the somewhat broader, mesoscale up- and down-welling motion that occurs at depths of 50–100 m. The submesoscale features appear in both the NH and HY models, suggesting that they are a HY phenomenon.

With the nonhydrostatic model and its hydrostatic counterpart, we are in a position to make careful comparisons between HY and NH model solutions. The solutions evolve differently, particularly when the resolution is high and the flows are wind forced. However, it proves to be difficult to identify categorical differences between the NH and HY model solutions at the scales resolved here. Most likely, greater resolution is required to enter the regime where the differences become apparent. It is conceivable that models achieving higher resolution will exhibit NH phenomena that remain unseen at the resolutions afforded here.

Acknowledgements

Thanks to J.C. McWilliams and A. Tandon for insightful discussions, and an anonymous reviewer for comments. This work was begun with ONR support (N00014-00-C-0079).

References

- Browning, G.L., Holland, W.R., Kreiss, H.-O., Worley, S.J., 1990. An accurate hyperbolic system for approximately hydrostatic and incompressible oceanographic flows. *Dynamics of Atmospheres and Oceans* 14, 303–332.
- Brugge, R., Jones, H.L., Marshall, J.C., 1991. Non-hydrostatic ocean modeling for studies of open-ocean deep convection. *Deep Convection and Deep Water Formation in the Oceans*. Elsevier Oceanography Series. Elsevier Sciences, New York, pp. 325–341.
- Chao, S.-Y., Shaw, P.-T., 2002. Nonhydrostatic aspects of coastal upwelling meanders and filaments off eastern ocean boundaries. *Tellus* 54A, 63–75.
- Dietrich, D., Lin, C.A., 2002. Effects of hydrostatic approximation and resolution on the simulation of convective adjustment. *Tellus* 54A, 34–43.
- Ferrari, R., Rudnick, D.L., 2000. The thermohaline structure of the upper ocean. *Journal of Geophysical Research* 105, 16,857–16,883.

- Fox-Kemper, B., Ferrari, R., Hallberg, R.W., 2006. Modeling and parameterizing mixed layer eddies. *Eos Trans. AGU* 87 (36), Ocean Sci. Meet. Suppl., Abstract OS23F-06.
- Haine, T.W.N., Williams, P.D., 2002. The role of nonhydrostatic dynamics in controlling development of a surface ocean front. *Ocean Modelling* 4, 121–135.
- Jones, Helen, Marshall, John, 1993. Convection with rotation in a neutral ocean: A study of open-ocean deep convection. *Journal of Physical Oceanography* 23 (6), 1009–1039.
- Kämpf, J., Backhaus, J.O., 1998. Shallow, brine-driven free convection in polar oceans: Nonhydrostatic numerical process studies. *Journal of Geophysical Research* 103 (C3), 5577–5593.
- Kasahara, A., 2003a. On the nonhydrostatic atmospheric models with inclusion of the horizontal component of the earth's angular velocity. *Journal of the Meteorological Society of Japan* 81 (5), 935–950.
- Kasahara, A., 2003b. The roles of horizontal component of the earth's angular velocity in nonhydrostatic linear models. *Journal of the Atmospheric Sciences* 30, 1085–1095.
- Large, W.G., McWilliams, J.C., Doney, S.C., 1994. Oceanic vertical mixing: A review and a model with a nonlocal boundary layer parameterization. *Reviews in Geophysics* 32, 363–403.
- Legg, S., Adcroft, A., 2003. Internal wave breaking at concave and convex continental slopes. *Journal of Physical Oceanography* 33, 2224–2246.
- Lévy, M., Klein, P., Treguier, A.-M., 2001. Impacts of sub-mesoscale physics on production and subduction of phytoplankton in an oligotrophic regime. *Journal of Marine Research* 59, 535–565.
- Mahadevan, A., Archer, D., 1998. Modeling a limited region of the ocean. *Journal of Computational Physics* 145 (2), 555–574.
- Mahadevan, A., Archer, D., 2000. Modeling the impact of fronts and mesoscale circulation on the nutrient supply and biogeochemistry of the upper ocean. *Journal of Geophysical Research* 105 (C1), 1209–1225.
- Mahadevan, A., Tandon, A., 2006. An analysis of mechanisms for submesoscale vertical motion at ocean fronts. *Ocean Modelling* 14 (3–4), 241–256.
- Mahadevan, A., Olinger, J., Street, R.L., 1996a. A non-hydrostatic mesoscale ocean model 1: Well-posedness and scaling. *Journal of Physical Oceanography* 26 (9), 1168–1880.
- Mahadevan, A., Olinger, J., Street, R.L., 1996b. A non-hydrostatic mesoscale ocean model 2: Numerical implementation. *Journal of Physical Oceanography* 26 (9), 1181–1900.
- Marshall, John, Hill, Chris, Perelman, Lev, Adcroft, Alistair, 1997. Hydrostatic, quasi-hydrostatic, and non-hydrostatic ocean modeling. *Journal of Geophysical Research* 102 (C3), 5733–5752.
- McWilliams, J.C., 2003. Diagnostic force balance and its limits, *Nonlinear Processes in Geophysical Fluid Dynamics*. Kluwer Academic Publishers., pp. 287–304.
- McWilliams, J.C., Molemaker, M.J., Yavneh, I., 2004. Ageostrophic, anticyclonic instability of a geostrophic barotropic boundary current. *Physics of Fluids* 16 (10), 3720–3725.
- Molemaker, M.J., McWilliams, J.C., Yavneh, I., 2005. Baroclinic instability and loss of balance. *Journal of Physical Oceanography* 35 (9), 1505–1517.
- Nagai, T., Tandon, A., Rudnick, D.L., 2006. Two dimensional ageostrophic secondary circulation at ocean fronts due to vertical mixing and large scale deformation. *Journal of Geophysical Research*, in press.
- Rudnick, Daniel L., 1996. Intensive surveys of the Azores front. Part II: Inferring the geostrophic and vertical velocity fields. *Journal of Geophysical Research* 101 (C7), 16291–16303.
- Sander, J., W-Gladrow, D., Olbers, D., 1995. Numerical studies of open ocean deep convection. *Journal of Geophysical Research* 100 (C10), 20579–20600.
- Song, Y.T., 1998. A general pressure gradient formulation for ocean models. Part I: Scheme design and diagnostic analysis. *Monthly Weather Review* 126, 3213–3230.
- Ullman, D.S., Cornillon, P.C., 1999. Satellite-derived sea surface temperature fronts on the continental shelf of the northeast US coast. *Journal of Geophysical Research* 104 (C10), 23459–23478.
- Winters, K.B., Seim, H.E., Finnigan, T.D., 2000. Simulation of non-hydrostatic, density-stratified flow in irregular domains. *International Journal of Numerical Methods in Fluids* 32, 263–284.
- Wunsch, C., Ferrari, R., 2004. Vertical mixing, energy and the general circulation of the oceans. *Annual Review of Fluid Mechanics* 36, 281–314.